ROYAL SOCIETY
OF CHEMISTRY

Journal of Materials Chemistry A

ARTICLE

Predicting two-dimensional pentagonal transition metal monophosphides for efficient electrocatalytic nitrogen reduction

Yiran Ying[a], Ke Fan[a], Xin Luo *[a,b], and Haitao Huang *[a]

Electrocatalytic reduction of nitrogen (N_2) to ammonia (NH_3), as an alternative to the traditional energy-consuming Habor–Bosch nitrogen fixation, is a fascinating yet challenging topic. Here, we design a novel group of materials—two-dimensional (2D) pentagonal transition metal phosphides (penta-MP, M=Ti, Zr, Hf) and study their potential applications in the nitrogen reduction reaction (NRR). Penta-MP are predicted to be dynamically, thermally, and mechanically stable through density functional theory calculation and *ab initio* molecular dynamics simulations. Their quasi-planar structures and metalic properties facilitate the strong N_2 adsorption on the surface. Gibbs free energy diagram suggests that NRR on penta-MP prefers the distal reaction mechanism, with the low overpotential of 0.56 eV for penta-TiP, which is beneficial for efficient electrocatalytic NRR. Our findings open up a new avenue for designing novel 2D materials as well as electrocatalysts.

1. Introduction

Ammonia (NH_3), which serves as a precursor of multifarious fertilizers, pharmaceuticals, refrigerants, and detergents, is undeniably an indispensable chemical in both agriculture and industry.[1-3] Besides, ammonia is also considered as a sustainable fuel and clean energy carrier, whose combustion only products environmentally benign water and dinitrogen (N_2).[4] Therefore, nitrogen fixation, which converts dinitrogen—the most abundant gas in the Earth's atmosphere (78%)—into ammonia, is a significant yet challenging topic in the field of chemistry as well as materials science. In industry, about 182 million tonnes of ammonia was synthesized in the world in 2017,[5] among which Haber–Bosch process plays the dominant role. Nevertheless, Haber–Bosch process with iron-based catalysts requires high temperature (about 500-700 K) and high pressure (up to 300 atm) to break the inert N≡N triple bond, making it very energy consuming, taking up about 1.4% of all energy consumption of human beings.[6-8]

Electrochemical nitrogen reduction reaction (NRR) with the general formula of $N_2+6H^++6e^- ->2NH_3$, which is first inspired by the biological nitrogen fixation by nitrogenases,[7] is a promising alternative for nitrogen fixation since the reaction can occur at ambient conditions and surmount the limitations of Haber–Bosch process—harsh reaction conditions, high energy consuming, large and complicated plant infrastructure, and environmental concerns.[9-12] The major challenge for electrochemical NRR lies in finding catalysts, which can effectively break the strong N≡N triple bond and

exhibit relatively low overpotentials for NRR.[9, 13] The past several years have witnessed the great efforts in overcoming this obstacle to facilitate effective electrochemical NRR. Metal[14-16], metal oxides[17], metal nitrides[18, 19], and single-atom catalysts[20-26] have been widely studied as NRR catalysts from the theoretical perspective using first-principles density functional theory (DFT) calculations, with some of the results confirmed by experiments.[27-30]

Two-dimensional (2D) materials, since its discovery, have been consistently examined as the electrocatalysts for hydrogen evolution reaction (HER), oxygen evolution reaction, and oxygen reduction reaction.[31] However, 2D materials for electrocatalytic NRR have not yet been fully explored theoretically or experimentally, except for a few examples. Azofra et al. used DFT results to suggest that 2D d^2-d^4 M_3C_2 transition metal carbides (MXenes) are promising candidates for NRR, exhibiting spontaneous N_2 chemisorption and an activation barrier of the rate-determining step (RDS) of only 0.64 eV for V_3C_2.[32] MXenes with another formula of M_2C/M_2N, especially Mo_2C, were also predicted to be promising candidates for NRR catalysts.[33] Li et al. predicted that MoN_2 nanosheets demonstrate excellent N_2 adsorption and activation performance, while doping with Fe resulted in good NRR reactivity with a calculated overpotential of 0.47 V.[34] In experiments, 2D boron-doped graphene was reported with remarkable NH_3 production rate of 9.8 µg·hr^{-1}·cm^{-1} with Faradic efficiency of 10.8% at -0.5 V (RHE) during NRR, which was well corroborated with DFT calculation results.[35] Luo et al. illustrated that MXene ($Ti_3C_2T_x$) nanosheets can achieve high faradic efficiency and low potential for NH_3 electrosynthesis, whose high activity can be attributed to more exposed edge sites, as predicted by DFT calculations.[36]

Recently, apart from traditional 2D materials which consist of hexagonal building blocks like graphene, transition metal dichalcogenides, and MXenes, a group of 2D pentagon-based materials has taken their turn in the spotlight. Intrinsic stabilities of

a. Department of Applied Physics, The Hong Kong Polytechnic University, Hung Hom, Kowloon, Hong Kong, P.R. China. E-mail: aphhuang@polyu.edu.hk
b. School of Physics, Sun Yat-sen University, Guangzhou, Guangdong Province, P.R. China, 510275. Email: luox77@mail.sysu.edu.cn

pentagonal graphene[37], SiC$_2$[38], CN$_2$[39], TiC$_2$[40], PdP$_2$/PdAs$_2$[41], Pt$_2$N$_4$[42], TMB/TMC[43], CrX (X=S, Se, Te)[44], and NiP$_2$[45] have been confirmed by theoretical calculations, while PdSe$_2$[46] was experimentally synthesized. Some 2D pentagonal materials exhibit novel physical and chemical properties due to their lowered symmetry, like negative Poisson's ratio for penta-graphene[37], high carrier mobilities for PdP$_2$/PdAs$_2$ and Pt$_2$N$_4$[41, 42], and are promising for future electronics applications. However, to the best of our knowledge, the applications of 2D pentagonal materials in electrocatalytic NRR have not been investigated before.

In this work, by means of first-principles DFT and molecular dynamics, we predict a new group of materials—2D pentagonal transition metal monophosphides (penta-MP, M=Ti, Zr, Hf) with dynamical, thermal, and mechanical stabilities. N$_2$ chemisorption on penta-MP and the subsequent activation of N≡N triple bond are predicted, while the metallic characteristics of penta-MP are maintained, which is beneficial to the electrocatalytic process. Furthermore, by calculating the Gibbs free energy changes for each elementary step in the NRR process using DFT, we demonstrate that penta-TiP exhibits low overpotential of 0.56 V. Our results provide new insights into the exploration of new 2D materials as well as the design of NRR electrocatalysts.

2. Computational methods

First-principles calculations were performed by applying the projector-augmented wave (PAW) scheme[47] within the Vienna ab initio Simulation Package (VASP)[48, 49] version 5.4.4. $3s3p4s3d$, $4s4p5s4d$, $5s5p6s5d$, $3p$, and $2p$ electrons were considered as valence electrons for Ti, Zr, Hf, P, and N, respectively. Generalized gradient approximation (GGA) with Perdew–Burke–Ernzerhof (PBE) parameterization[50] was used as the exchange-correlation functional. Grimme's DFT-D3 scheme[51] was adopted to account for the van der Waals interactions throughout the calculations. Kinetic energy cut-off for all calculations was set as 450 eV. A Monkhorst–Pack 11×11×1 and 5×5×1 mesh[52] was used to sample for integration over the first Brillouin zone for the unit cell and 2×2 supercell, respectively. During density of state (DOS) calculations for the 2×2 supercell, however, a much denser 9×9×1 mesh was applied. The structures were allowed to relax until the total energy was less than $1×10^{-6}$ eV and Hellmann-Feynman force was less than 0.01 eV/Å. Vacuum layers with a thickness of at least 15 Å were used to avoid interactions between adjacent cells. Crystal structures and charge density distributions were visualized with VESTA.[53]

Phonon dispersion was calculated from 3×3×1 supercells using the density functional perturbation theory (DFPT) implemented in the PHONOPY code[54] interfaced with VASP. During phonon dispersion calculations, the energy and force convergence criteria were set as $1×10^{-8}$ eV and 0.001 eV/Å, and local density approximation (LDA) to the exchange-correlation functional was employed. *Ab initio* molecular dynamics (AIMD) were performed by adopting the canonical (NVT) ensemble with Nosé algorithm[55], as implemented in VASP.

Adsorption energies of adsorbate X on penta-MP were calculated using the formula:

$$E_{ads}=E(MP/X)-E(MP)-E(X)$$

where E(MP), E(X), and E(MP/X) represent the DFT-calculated energies of the clean surface, the adsorbate, and the system including the adsorbed molecule, respectively.

Theoretically, NRR was considered as a six net coupled proton and electron transfer (CPET) process (N$_2$+6H$^+$+6e$^-$->2NH$_3$)[14] with one proton and coupled electron transferred from the solution onto the surface of the catalysts for each step, and Gibbs free energy changes for all intermediates during which were calculated as:[56]

$$ΔG=ΔE_{DFT}+ΔE_{ZPE}-TΔS+ΔG_{pH}$$

where $ΔE_{DFT}$, $ΔE_{ZPE}$, $TΔS$, and $ΔG_{pH}$ represent the difference of DFT-calculated adsorption energy, zero point energy (ZPE), entropic contribution, and free energy correction of pH. Gibbs free energy for H$^+$+e$^-$ was calculated through the standard hydrogen electrode model to simulate the anode reaction (H$_2$⇌2(H$^+$+e$^-$))[14, 22, 57]:

$$G(H^++e^-)=0.5G(H_2)-eU$$

where U represents the applied electrode potential in the model. In other words, the proton source in theoretical calculations is the gaseous H$_2$. More details on the Gibbs free energy calculation can be found in Table S3-S6 in the Electronic Supplementary Information (ESI).

3. Results and discussion

3.1 Crystal structures, stabilities, elastic and electronic properties

A representative crystal structure of 2D pentagonal MP (denoted as penta-MP, M=Ti, Zr, Hf) is shown in Fig. 1a. Penta-MP possesses the space group of p4/mbm, and their first Brillouin zone (BZ) with high-symmetry points is plotted in Fig. 1b. Top view of the crystal structure of 2D penta-MP shows a typical shape of Cairo pentagonal tiling, the unit cell of which is formed by four pentagon rings, and each ring consists of three transition metal atoms and two phosphorus atoms. Unlike planar 2D pentagonal PdP$_2$, PdAs$_2$[41], and Pt$_2$N$_4$[42] structures, side view of penta-MP in Fig. 1a exhibits the quasi-planar characteristic, with one layer of transition metal atoms sandwiched by two symmetric layers of phosphorus atoms. Lattice constant a, bond lengths between M-P (denoted as d_1), M-M (d_2), P-P (h), and bond angles M-M-P (α), M-P-M (β), and P-M-P (γ) marked in Fig. 1a of penta-TiP, penta-ZrP, and penta-HfP are listed in Table S1. Similar to penta-PdSe$_2$[46], this puckered, quasi-planar structure of penta-MP is formed to maintain the symmetry of pentagonal lattice, providing abundant adsorption sites which may lead to multiple energy-related applications.

Before discussing other properties, we first need to examine the stability of penta-MP (M=Ti, Zr, Hf). The phonon dispersion spectra of penta-MP are calculated by DFPT and shown in Fig. 1c-1e, in which we can observe that the low-frequency optical and acoustic branches are well-separated from each other in gamma point and no imaginary phonon frequencies can be seen in the entire BZ, indicating the dynamical stability of penta-TiP, penta-ZrP, and penta-HfP. 2D pentagonal group 5 (V, Nb, Ta) and group 6 (Cr, Mo, W) transition metal monophosphides with the same space group and similar crystal structures, on the other hand, are not dynamically stable due to large imaginary frequencies (Fig. S1 in the ESI), thus are not discussed in the following sections.
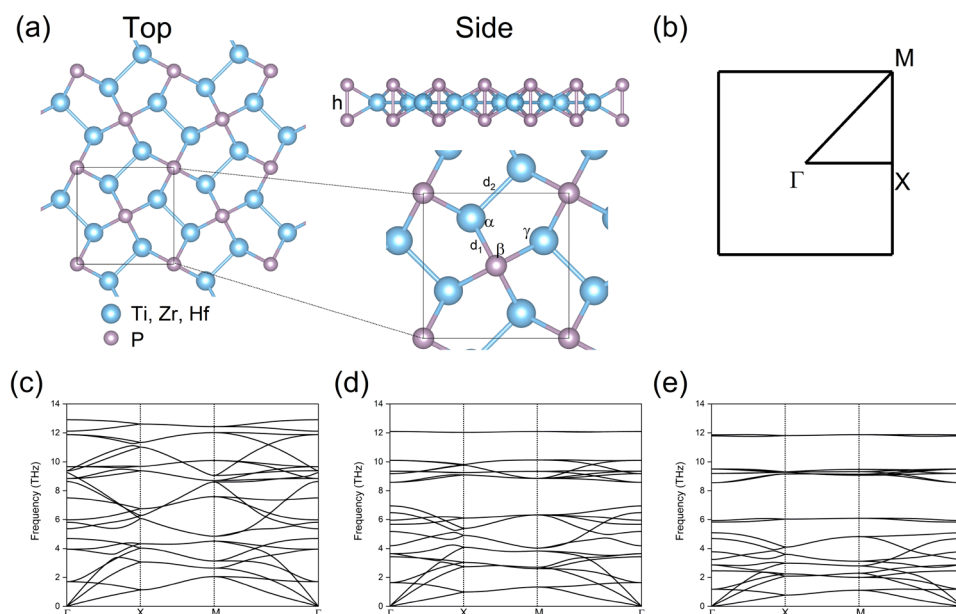
Fig. 1 (a) Top (left) and side (right) views of crystal structure of penta-MP (M=Ti, Zr, Hf), (b) the first Brillouin zone and high-symmetry points of penta-MP, the phonon dispersion spectra of (c) penta-TiP, (d) penta-ZrP, and (e) penta-HfP.

To confirm the thermal stabilities of penta-MP, we perform AIMD simulations with NVT ensemble under the temperature of 300 K. In the 3×3×1 supercells simulation box, the total energies as a function of time during AIMD simulations (Fig. 2) reach their equilibrium values quickly and oscillate within a small range. Snapshots of the structures after 10 ps (inset of Fig. 2a-c) show no obvious structural reconstructions after the AIMD simulations, suggesting that penta-MPs are thermally stable under ambient temperature.

By calculating the Hessian matrices along each Cartesian directions, we derive the three-dimensional elastic constants using the strain-stress relations.[58, 59] 2D elastic constants obtained from renormalization by multiply the thickness of vacuum layer[60, 61] are summarized in Table S2. Due to the symmetry, $C_{11}=C_{22}$, and only three elastic constants are independent for penta-MP: C_{11}, C_{12}, and C_{66} (using the Voigt notation 1-xx, 2-yy, and 6-xy[62]). For all three structures, criteria for mechanical stability ($C_{11}C_{22}-C_{12}^2>0$, $C_{66}>0$)[63] are satisfied. Furthermore, we calculate the orientation-dependent Young's moduli and Poisson's ratios (details can be found in the ESI).

As shown in Fig. S2, for all structures, Young's moduli reach the minimum values at θ=0° (x direction), and maximum ones at θ=45° (diagonal direction). Poisson's ratios, on the other hand, reach the maximum along x direction and minimum along the diagonal direction (values are listed in Table S1). The wide range of Young's modulus and Poisson's ratio with different orientation indicates high mechanical anisotropy of penta-MP.

Bader charge analysis[64] confirms that electrons transfer from transition metal atoms to P, with the charge transfer values listed in Table S2. To illustrate the electronic properties of penta-MP, we further calculate the density of states (DOS) and band structures (Fig. 3a, S3, and S4). Projected DOS for penta-MP in Fig. 3a and S3 can clearly manifest the metallicity for all three systems, which is mainly contributed by the 3d orbital of transition metal atoms. We further consider the influence of spin-orbit coupling (SOC) effect on the electronic
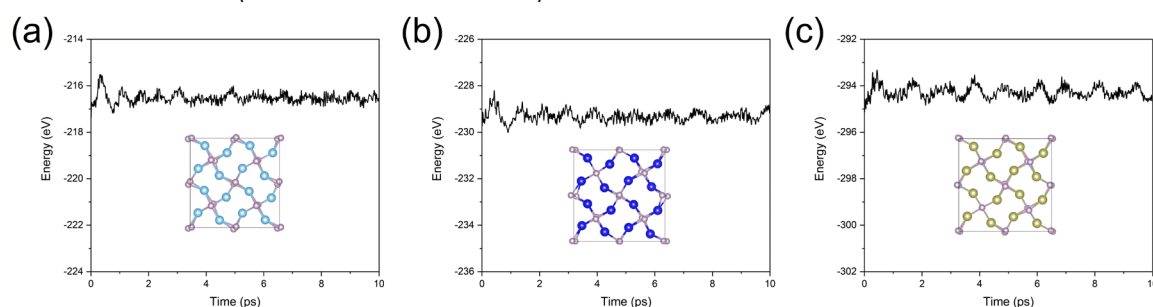

Fig. 2 Total energy as a function of time under the temperature of 300 K during AIMD simulations for (a) penta-TiP, (b) penta-ZrP, and (c) penta-HfP. Insets: snapshots of crystal structure after 10 ps AIMD simulations. (Ti, Zr, Hf, and P atoms are represented in cyan, blue, brownish yellow, and purple, respectively.)
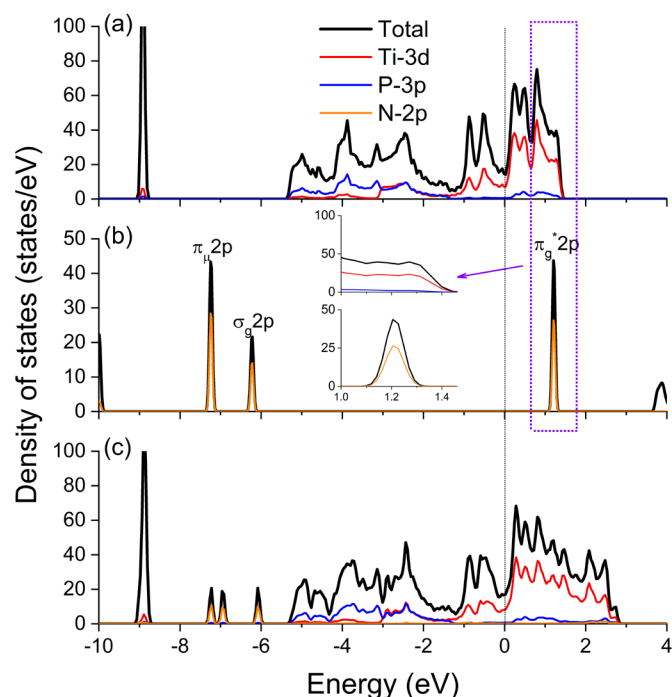
Fig. 3 Partial density of states (DOS) for (a) penta-TiP in 2×2 supercell ($Ti_{16}P_{16}$), (b) N_2 molecule in the gas phase, and (c) penta-TiP in 2×2 supercell with one adsorbed N_2 molecule ($Ti_{16}P_{16}N_2$). Fermi level is set to zero (denoted by the dotted line). Enlarged view of (a) and (b) is shown in inset.

properties of penta-MP. Band structures calculated with or without SOC effect show very little difference even for penta-HfP with heavy atom Hf (Fig. S5). Thus, for computational convenience, SOC effect is not included in the following calculations. In addition, we use HSE06 hybrid functionals with the fraction of local exact exchange of 0.25[65, 66] to obtain more rigorous band structures (Fig. S6). The metallicity of penta-MP can be confirmed, which can facilitate electron transfer and is beneficial for the potential electrocatalytic applications.

3.2 N_2 chemisorption

To design an efficient catalyst for NRR, the N_2 chemisorption always remains the first and vital consideration.[14, 22, 67] Transition metal-based catalysts for NRR with both occupied and unoccupied d orbitals, such as group 4 metals with d^2 configuration in this study, are promising for the chemisorption of N_2 and activation of chemically inert N≡N triple bond. This can be ascribed to the 'acceptance-donation' mechanism[67, 68]: occupied d electrons of TM atom can be donated to the antibonding orbital of N_2, while unoccupied d orbitals can accept lone-pair electrons from N_2. In this concern, we investigate the N_2 chemisorption on the surface of penta-MP.

After fully relaxing atomic positions and calculating adsorption energies for both side-on and end-on configurations on different adsorption sites on the surface of penta-MP, we find that for all the three systems, only end-on chemisorption pattern can be realized (Fig. 4a and Fig. S7), with the adsorption energies of -0.51, -0.79, and -0.69 eV for penta-TiP, penta-ZrP,

and penta-HfP, respectively, indicating that the chemisorption of N_2 on penta-MP is an energetically favorable process. The corresponding N-N bond lengths are elongated to 1.16, 1.17, and 1.15 Å, respectively, compared with 1.098 Å for N_2 in the gas phase.[69] Moreover, Bader charge analysis shows that two nitrogen atoms gain 0.60 and 0.30 |e| from penta-TiP (Fig. 4a). Similar results can be obtained for penta-ZrP (0.75 and 0.34 |e|) and penta-HfP (0.67 and 0.20 |e|), as presented in Fig. S5. The values are much larger than the reported values for N_2 adsorbed on Mo-BN monolayer (0.29 |e| for two nitrogen atoms in total)[22] and $Mo_1-N_1C_2$ (0.49 |e| in total)[70]. These results indicate that the inert N≡N triple bonds can be effectively activated.

To unravel the mechanisms for the bond activation and obtain a better view of charge transfer and bonding character during the N_2 chemisorption, we calculate the charge density difference distribution Δρ of penta-TiP+N_2 as an example using the formula Δρ=ρ(penta-MP+N_2)-ρ(penta-MP)-ρ(N_2), as plotted in Fig. 4b and 4c. Charge accumulation (yellow) and depletion (cyan) can be observed for both the N_2 molecule and the Ti atom adjacent to it. This gives a clear indication that charge transfer between penta-TiP and N_2, which confirms the 'acceptance-donation' mechanism, i.e., Ti accepts lone-pair electrons from N_2 and donates electrons to N_2 simultaneously. We also plot the electron localization functions (ELF) for slices along (001) planes, one with the adsorbed N atom adjacent to Ti atoms (Fig. 4d) and the other including Ti atoms (Fig. 4e). From Fig. 4e, we can conclude that electrons are strongly localized around the Ti atoms since the corresponding regions have ELF values greater than 0.9 (the red regions). For the adsorbed N atom (Fig. 4e), on the other hand, electrons are strongly delocalized, with the ELF values close to 0.5 (the green region).

In addition, we perform the electronic structure calculations, with the total and N-2p projected DOS for N_2 in the gas phase shown in Fig. 3b. The highest occupied molecular orbital (HOMO) and lowest unoccupied molecular orbital (LUMO) for N_2 are located at the $\sigma_g 2p$ and $\pi_g^* 2p$ orbital, respectively,[71] which are marked in the figure. The d orbital of Ti and $\pi_g^* 2p$ orbital of N with matched energy levels overlap with each other, leading to the highly delocalized d-π* orbitals (Fig. 3c), which is responsible for the activation of N_2.

3.3 Electrocatalytic nitrogen reduction mechanisms

We proceed to analyze the NRR catalytic performance for penta-MP (M=Ti, Zr, Hf). Taking the N_2 adsorption configuration into account, two nitrogen reduction mechanisms, i.e., distal and alternating mechanisms are considered (Fig. 5).[22, 67] In reaction pathways for both mechanisms, six consecutive protonation steps are included, forming two ammonia molecules with the general formula of $N_2+6H^++6e->2NH_3$. By AIMD simulations, we note that in such an acidic aqueous solution, penta-MP can sustain the crystal structures without decomposition (Fig. S8).

We calculate the Gibbs free energies of all possible intermediates in NRR for penta-MP by adding the zero point energy and entropic corrections to the DFT-calculated energies. Free energy diagrams are shown in Fig. 6 and Fig. S9. The first
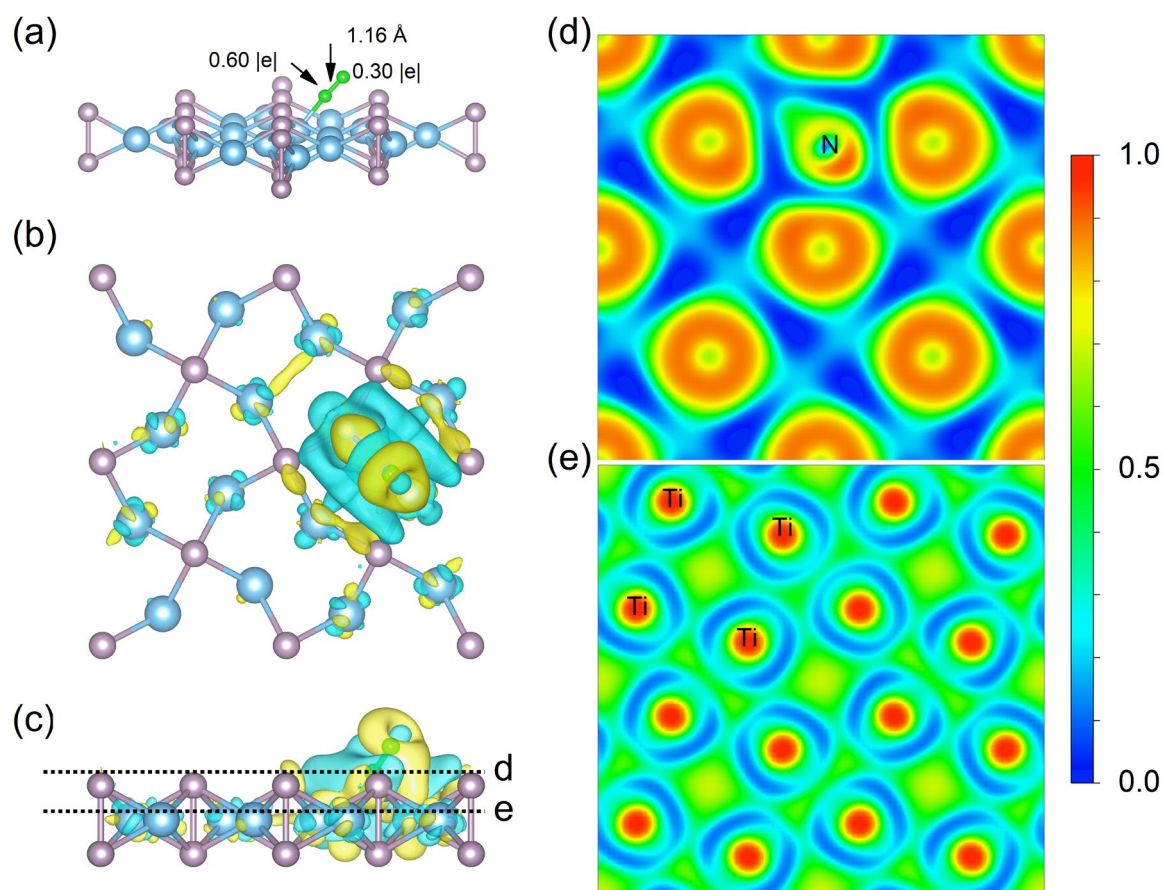
This journal is © The Royal Society of Chemistry 2019

J. Mater. Chem. A, 2019, **00**, 1-8 | **4**

Fig. 4 (a) Optimized structure of one N_2 molecule adsorbed on the surface of penta-TiP (2×2 supercell, cyan: Ti; purple: P; green: N) with the corresponding charge density difference distribution $\Delta\rho$ from (b) top and (c) side view (charge accumulation and depletion are shown in yellow and cyan), and selected slices (d) and (e) for plotting the electron localization function (ELF). The sliced planes d and e are indicated by dashed lines in (c). The right panel with the color map shows the isodensity values.

step involves the formation of intermediate *N=NH. For penta-TiP, the hydrogen is attached to the distal N site with the N-H bond length of 1.04 Å, and the N-N bond length is elongated from 1.16 Å to 1.25 Å, with the free energy change of 0.38 eV. For distal and alternating mechanism, the second step forms different intermediates of *NH=NH and *N-NH$_2$. The latter one is more energetically favorable, with the Gibbs free energy 1.77 eV lower than the former. The N-N bond for TiP-N-NH$_2$ is further extended to 1.32 Å, and the Gibbs free energy change is -0.47 eV. In the third step, *N+NH$_3$ is preferred rather than *NH-NH$_2$, thus, the first ammonia molecule is released in this step. Subsequently, three protons attack *N to form the second ammonia molecule. The overall Gibbs energy diagram (Fig. 5) shows that for penta-TiP, only the first (*N≡N->*N=NH) and the sixth (*NH$_2$->*NH$_3$) protonation steps are endothermic and the other ones are all exothermic. For penta-ZrP and penta-HfP, on the other hand, the second step (*N=NH->*N-NH$_2$) is also endothermic, albeit they prefer the same distal pathway as penta-TiP (Fig. S9). Along the distal reaction pathway, the highest barrier for penta-TiP, penta-ZrP, and penta-HfP lies in the sixth protonation step, i.e. *NH$_2$->*NH$_3$, with the energy barriers of 0.72, 0.88, and 1.00 eV, respectively, which can be identified as the potential-determining step (PDS). Upon an applied potential of U_{PDS}=-0.72 V, all steps in the NRR process

can be endothermic for penta-TiP, with the values of Gibbs free energy change for each step negative (Fig. 6).

The overpotential η is further calculated as $\eta=U_{equilibrium}-U_{PDS}$, with the equilibrium potential of NRR set as -0.16 V.[22, 70] Penta-TiP exhibit the smallest overpotential of 0.56 V, lower than that for the well-established (100) facet of rocksalt ZrN (0.60 V).[19] Approaches such as iron doping[25, 34] or single-atom embedding[22-24] might further optimize the overpotential for effective NRR applications. In addition, we plot the variation of Bader charge transfer values along the distal pathway for penta-TiP (Fig. S10). In general, penta-TiP serves as the electron reservoir, donating around 1 |e| to the adsorbates during the NRR process.
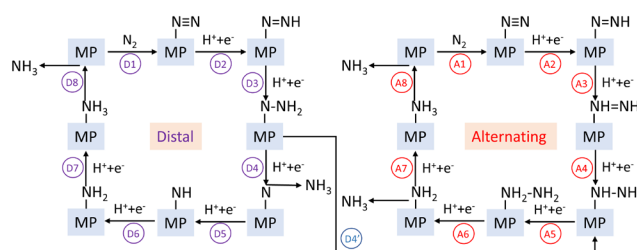

Fig. 5 Schematic illustration of distal and alternating mechanisms for nitrogen reduction on penta-MP.

This journal is © The Royal Society of Chemistry 2019

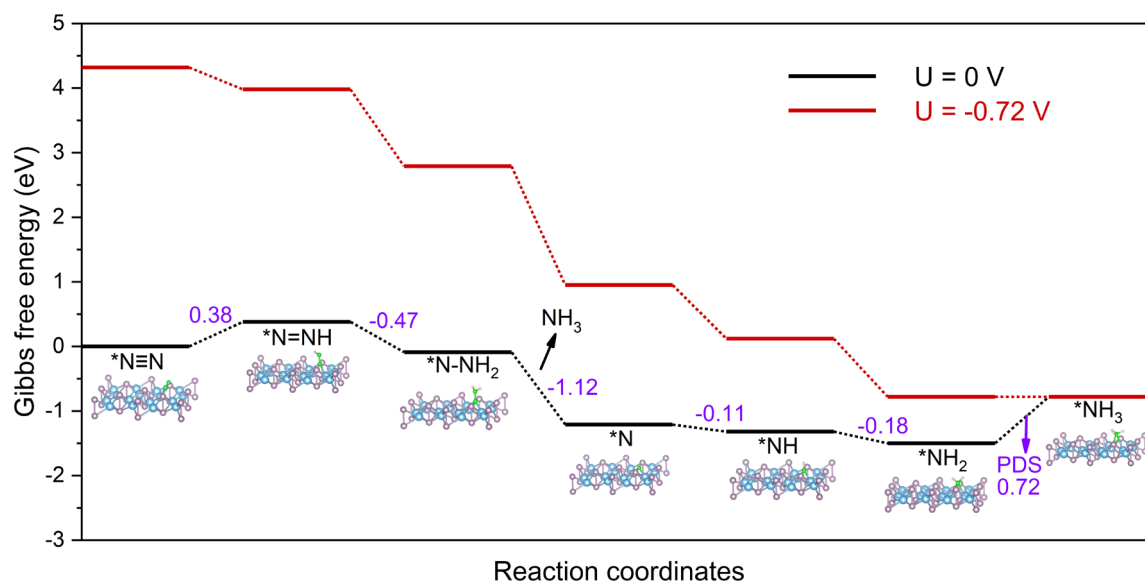*J. Mater*. Chem. A, 2019, **00**, 1-8 | **5**

Fig. 6 Gibbs free energy diagram for nitrogen reduction reaction on penta-TiP at zero and applied potential U through the distal mechanism. Crystal structures of all intermediates are also shown (Cyan: Ti; purple: P; green: N; pink: H). Relative Gibbs free energy changes for each step under U=0 are marked and shown in the unit of eV.

To ensure the reliability of calculated Gibbs free energy and overpotentials from PBE functional with DFT-D3 vdW corrections, we test the overpotentials calculated by a more sophisticated meta-GGA functional, revised TPSS (RTPSS), which was reported to give a better description of adsorption energies (Table S7, S10, and S11).[72] We also examine the results with PBE functional but different vdW correction schemes, including DFT-D2[73] and optB86b-vdW[74] (Table S8-S11). We find that different functionals and vdW correction types do not change the preference of N_2 chemisorption, the PDS of NRR (*NH_2->*NH_3), as well as the preferred reaction pathways, but affect the calculated N_2 adsorption energies (Table S10) and overpotentials (Table S11). Under RTPSS functional, the overpotential of 0.52 eV for penta-TiP is predicted, very close to the PBE-calculated overpotential value, confirming the validity of our calculations.

Finally, we would like to discuss the fundamental insights into the low NRR overpotentials for penta-MP. Nørskov and co-workers used a volcano-shape plot to relate the NRR overpotentials to the binding energy of N adatoms.[9, 14, 75] The overpotentials of NRR catalysts which bind nitrogen too strongly are limited by the step *NH_2->*NH_3 (stepped surfaces) or *NH->*NH_2 (flat surfaces) while those of NRR catalysts which bind nitrogen too weakly are limited by the step *N_2->*N_2H.[9, 10, 14] The calculated binding energies of N on penta-TiP, penta-ZrP, and penta-HfP are -0.87 eV, -0.80 eV, and -1.14 eV respectively (bind strongly), while the PDS for penta-MP from our calculations is *NH_2->*NH_3, which is in agreement with Nørskov's results. These binding energies lie near the top of the volcano plot and are very close to that for good NRR catalysts

like Ru (111)[9], indicating that the binding strength between the substrate and adsorbed N is neither too strong nor too weak, which can benefit the low overpotential of penta-MP.

Since HER is considered as a major competing reaction for NRR,[10, 75] we also calculate the single H atom adsorption free energies ΔG_H on penta-MP, which is an important indicator of HER performance (Fig. S11). Under zero potential, the adsorption of H on penta-MP is too strong (ΔG_H<0), and the desorption of H is the HER rate-limiting step[75]. The applied potential values of NRR (e.g. U=-0.72 V for penta-TiP) will further facilitate the adsorption and desorption of H to form H_2 requires large energy input, which leads to poor HER activity and high selectivity of NRR instead of HER. Combined with the high electrical conductivity (metallic character), strong N_2 adsorption, and low theoretical overpotentials, penta-MP structures have promising applications as NRR catalysts.

4. Conclusions

To summarize, by means of density functional theory and *ab initio* molecular dynamics calculations, we predict a group of new 2D materials—pentagonal transition metal monophosphides (penta-MP, M=Ti, Zr, Hf) for the electrocatalytic nitrogen reaction. These penta-MP show metallic behaviors with robust dynamical, thermal, and mechanical stabilities. The quasi-planar crystal structures and intrinsic electronic structures of penta-MP facilitate strong N_2 adsorption on their surface through the 'acceptance-donation' mechanism due to the hybridization between transition metal-d and nitrogen-π* orbitals. Moreover, the DFT-calculated Gibbs

free energy changes during NRR process suggest that nitrogen reduction on penta-MP prefers the distal reaction pathway. In particular, a low overpotential of 0.56 eV is predicted for penta-TiP. Our results reveal that the novel pentagonal two-dimensional materials may find their potential applications in electrocatalysis and energy-related materials.

Conflicts of interest

There are no conflicts of interest to declare.

Acknowledgements

References

1. V. Smil, *Nature*, 1999, **400**, 415.
2. J. N. Galloway, A. R. Townsend, J. W. Erisman, M. Bekunda, Z. C. Cai, J. R. Freney, L. A. Martinelli, S. P. Seitzinger and M. A. Sutton, *Science*, 2008, **320**, 889-892.
3. J. Postgate, *The chemistry and biochemistry of nitrogen fixation*, Springer Science & Business Media, 2012.
4. C. Zamfirescu and I. Dincer, *J. Power Sources*, 2008, **185**, 459-465.
5. J. A. Ober, *Mineral commodity summaries 2018*, US Geological Survey, 2018.
6. S. Giddey, S. P. S. Badwal and A. Kulkarni, *Int. J. Hydrogen Energy*, 2013, **38**, 14576-14594.
7. C. J. van der Ham, M. T. Koper and D. G. Hetterscheid, *Chem. Soc. Rev.*, 2014, **43**, 5183-5191.
8. B. M. Hoffman, D. Lukoyanov, Z. Y. Yang, D. R. Dean and L. C. Seefeldt, *Chem. Rev.*, 2014, **114**, 4041-4062.
9. J. H. Montoya, C. Tsai, A. Vojvodic and J. K. Norskov, *ChemSusChem*, 2015, **8**, 2180-2186.
10. C. Guo, J. Ran, A. Vasileff and S.-Z. Qiao, *Energy Environ. Sci.*, 2018, **11**, 45-56.
11. X. Cui, C. Tang and Q. Zhang, *Adv. Energy Mater.*, 2018, **8**, 1800369.
12. S. L. Foster, S. I. P. Bakovic, R. D. Duda, S. Maheshwari, R. D. Milton, S. D. Minteer, M. J. Janik, J. N. Renner and L. F. Greenlee, *Nature Catal.*, 2018, **1**, 490-500.
13. A. R. Singh, B. A. Rohr, J. A. Schwalbe, M. Cargnello, K. Chan, T. F. Jaramillo, I. Chorkendorff and J. K. Nørskov, *ACS Catal.*, 2016, **7**, 706-709.
14. E. Skulason, T. Bligaard, S. Gudmundsdottir, F. Studt, J. Rossmeisl, F. Abild-Pedersen, T. Vegge, H. Jonsson and J. K. Norskov, *Phys. Chem. Chem. Phys.*, 2012, **14**, 1235-1245.
15. S. Back and Y. Jung, *Phys. Chem. Chem. Phys.*, 2016, **18**, 9161-9166.
16. J. G. Howalt, T. Bligaard, J. Rossmeisl and T. Vegge, *Phys. Chem. Chem. Phys.*, 2013, **15**, 7785-7795.
17. Á. B. Höskuldsson, Y. Abghoui, A. B. Gunnarsdóttir and E. Skúlason, *ACS Sustainable Chem. Eng.*, 2017, **5**, 10327-10333.
18. Y. Abghoui, A. L. Garden, J. G. Howalt, T. Vegge and E. Skúlason, *ACS Catal.*, 2015, **6**, 635-646.
19. Y. Abghoui, A. L. Garden, V. F. Hlynsson, S. Bjorgvinsdottir, H. Olafsdottir and E. Skulason, *Phys. Chem. Chem. Phys.*, 2015, **17**, 4909-4918.
20. Y. Q. Le, J. Gu and W. Q. Tian, *Chem. Commun.*, 2014, **50**, 13319-13322.
21. X. F. Li, Q. K. Li, J. Cheng, L. Liu, Q. Yan, Y. Wu, X. H. Zhang, Z. Y. Wang, Q. Qiu and Y. Luo, *J. Am. Chem. Soc.*, 2016, **138**, 8706-8709.
22. J. Zhao and Z. Chen, *J. Am. Chem. Soc.*, 2017, **139**, 12480-12487.
23. Z. Wang, Z. Yu and J. Zhao, *Phys. Chem. Chem. Phys.*, 2018, **20**, 12835-12844.
24. J. Zhao, J. Zhao and Q. Cai, *Phys. Chem. Chem. Phys.*, 2018, **20**, 9248-9255.
25. Z. Wei, Y. Zhang, S. Wang, C. Wang and J. Ma, *J. Mater. Chem. A*, 2018, **6**, 13790-13796.
26. X. Chen, X. Zhao, Z. Kong, W.-J. Ong and N. Li, *J. Mater. Chem. A*, 2018, **6**, 21941-21948.
27. S. Licht, B. Cui, B. Wang, F.-F. Li, J. Lau and S. Liu, *Science*, 2014, **345**, 637-640.
28. R. Lan, J. T. Irvine and S. Tao, *Sci. Rep.*, 2013, **3**, 1145.
29. X. Ren, G. Cui, L. Chen, F. Xie, Q. Wei, Z. Tian and X. Sun, *Chem. Commun.*, 2018, **54**, 8474-8477.
30. Z. Geng, Y. Liu, X. Kong, P. Li, K. Li, Z. Liu, J. Du, M. Shu, R. Si and J. Zeng, *Adv. Mater.*, 2018, **30**, 1803498.
31. H. Jin, C. Guo, X. Liu, J. Liu, A. Vasileff, Y. Jiao, Y. Zheng and S. Z. Qiao, *Chem. Rev.*, 2018, **118**, 6337-6408.
32. L. M. Azofra, N. Li, D. R. MacFarlane and C. Sun, *Energy Environ. Sci.*, 2016, **9**, 2545-2549.
33. M. Shao, Y. Shao, W. Chen, K. L. Ao, R. Tong, Q. Zhu, I. N. Chan, W. F. Ip, X. Shi and H. Pan, *Phys. Chem. Chem. Phys.*, 2018, **20**, 14504-14512.
34. Q. Li, L. He, C. Sun and X. Zhang, *J. Phys. Chem. C*, 2017, **121**, 27563-27568.
35. X. Yu, P. Han, Z. Wei, L. Huang, Z. Gu, S. Peng, J. Ma and G. Zheng, *Joule*, 2018, **2**, 1610-1622.
36. Y. Luo, G.-F. Chen, L. Ding, X. Chen, L.-X. Ding and H. Wang, *Joule*, 2019, **3**, 279-289.
37. S. H. Zhang, J. Zhou, Q. Wang, X. S. Chen, Y. Kawazoe and P. Jena, *Proc. Natl. Acad. Sci. U. S. A.*, 2015, **112**, 2372-2377.
38. A. Lopez-Bezanilla and P. B. Littlewood, *J. Phys. Chem. C*, 2015, **119**, 19469-19474.
39. S. Zhang, J. Zhou, Q. Wang and P. Jena, *J. Phys. Chem. C*, 2016, **120**, 3993-3998.
40. T. Zhao, S. Zhang, Y. Guo and Q. Wang, *Nanoscale*, 2016, **8**, 233-242.
41. H. Yuan, Z. Li and J. Yang, *J. Mater. Chem. C*, 2018, **6**, 9055-9059.
42. Z. Liu, H. Wang, J. Sun, R. Sun, Z. F. Wang and J. Yang, *Nanoscale*, 2018, **10**, 16169-16177.
43. Y. Shao, M. Shao, Y. Kawazoe, X. Shi and H. Pan, *J. Mater. Chem. A*, 2018, **6**, 10226-10232.
44. W. Chen, Y. Kawazoe, X. Shi and H. Pan, *Phys. Chem. Chem. Phys.*, 2018, **20**, 18348-18354.
45. X. Shao, X. Liu, X. Zhao, J. Wang, X. Zhang and M. Zhao, *Phys. Rev. B*, 2018, **98**, 085437.

This journal is © The Royal Society of Chemistry 2019

J. Mater. Chem. A, 2019, **00**, 1-8 | **7**

46. A. D. Oyedele, S. Yang, L. Liang, A. A. Puretzky, K. Wang, J. Zhang, P. Yu, P. R. Pudasaini, A. W. Ghosh, Z. Liu, C. M. Rouleau, B. G. Sumpter, M. F. Chisholm, W. Zhou, P. D. Rack, D. B. Geohegan and K. Xiao, *J. Am. Chem. Soc.*, 2017, **139**, 14090-14097.
47. P. E. Blöchl, *Phys. Rev. B*, 1994, **50**, 17953-17979.
48. G. Kresse and J. Furthmuller, *Phys. Rev. B*, 1996, **54**, 11169-11186.
49. G. Kresse and J. Furthmuller, *Comput. Mater. Sci.*, 1996, **6**, 15-50.
50. J. P. Perdew, K. Burke and M. Ernzerhof, *Phys. Rev. Lett.*, 1996, **77**, 3865-3868.
51. S. Grimme, J. Antony, S. Ehrlich and H. Krieg, *J. Chem. Phys.*, 2010, **132**, 154104.
52. H. J. Monkhorst and J. D. Pack, *Phys. Rev. B*, 1976, **13**, 5188-5192.
53. K. Momma and F. Izumi, *J. Appl. Crystallogr.*, 2011, **44**, 1272-1276.
54. A. Togo and I. Tanaka, *Scripta Mater.*, 2015, **108**, 1-5.
55. S. Nosé, *J. Chem. Phys.*, 1984, **81**, 511-519.
56. A. A. Peterson, F. Abild-Pedersen, F. Studt, J. Rossmeisl and J. K. Nørskov, *Energy Environ. Sci.*, 2010, **3**, 1311-1315.
57. J. K. Norskov, J. Rossmeisl, A. Logadottir, L. Lindqvist, J. R. Kitchin, T. Bligaard and H. Jonsson, *J. Phys. Chem. B*, 2004, **108**, 17886-17892.
58. Y. Le Page and P. Saxe, *Phys. Rev. B*, 2002, **65**, 104104.
59. Y. Ying, X. Luo and H. Huang, *J. Phys. Chem. C*, 2018, **122**, 17718-17725.
60. M. N. Blonsky, H. L. L. Zhuang, A. K. Singh and R. G. Hennig, *ACS Nano*, 2015, **9**, 9885-9891.
61. A. Rawat, N. Jena, D. Dimple and A. De Sarkar, *J. Mater. Chem. A*, 2018, **6**, 8693-8704.
62. R. C. Andrew, R. E. Mapasha, A. M. Ukpong and N. Chetty, *Phys. Rev. B*, 2012, **85**, 125428.
63. F. Mouhat and F.-X. Coudert, *Phys. Rev. B*, 2014, **90**, 224104.
64. W. Tang, E. Sanville and G. Henkelman, *J. Phys.: Condens. Matter*, 2009, **21**, 084204.
65. J. Heyd, G. E. Scuseria and M. Ernzerhof, *J. Chem. Phys.*, 2003, **118**, 8207-8215.
66. A. V. Krukau, O. A. Vydrov, A. F. Izmaylov and G. E. Scuseria, *J. Chem. Phys.*, 2006, **125**, 224106.
67. C. Ling, X. Niu, Q. Li, A. Du and J. Wang, *J. Am. Chem. Soc.*, 2018, **140**, 14161-14168.
68. M.-A. Légaré, G. Bélanger-Chabot, R. D. Dewhurst, E. Welz, I. Krummenacher, B. Engels and H. Braunschweig, *Science*, 2018, **359**, 896-900.
69. W. M. Haynes, *CRC handbook of chemistry and physics*, CRC press, 2014.
70. C. Ling, X. Bai, Y. Ouyang, A. Du and J. Wang, *J. Phys. Chem. C*, 2018, **122**, 16842-16847.
71. J. C. Liu, X. L. Ma, Y. Li, Y. G. Wang, H. Xiao and J. Li, *Nat. Commun.*, 2018, **9**, 1610.
72. J. Sun, M. Marsman, G. I. Csonka, A. Ruzsinszky, P. Hao, Y.-S. Kim, G. Kresse and J. P. Perdew, *Phys. Rev. B*, 2011, **84**, 035117.
73. S. Grimme, *J. Comput. Chem.*, 2006, **27**, 1787-1799.
74. J. Klimeš, D. R. Bowler and A. Michaelides, *Phys. Rev. B*, 2011, **83**, 195131.
75. Z. W. Seh, J. Kibsgaard, C. F. Dickens, I. Chorkendorff, J. K. Norskov and T. F. Jaramillo, *Science*, 2017, **355**, eaad4998.

This journal is © The Royal Society of Chemistry 2019

J. Mater. Chem. A, 2019, **00**, 1-8 | **8**